RESEARCH ARTICLE

Check for updates

Multicolor and multimodal luminescence in an Er[3+] single-doped double perovskite for advanced anti-counterfeiting and encryption†

Sixia Li,[a,b] Peng Zhang,[a] Zhenbing Wang,[b] Yuzhu Yang,[a] Xuan Miao[a] and Weisheng Liu ✱[a,b]

Multicolor and multimodal luminescence materials play crucial roles in anti-counterfeiting and encryption technologies due to their attractive properties of colorful, visually identifiable emissions and distinct emission modes in various excitation or stimulus channels. Nevertheless, integrating multicolor and multimodal luminescence *via* single rare-earth doping based on a single matrix remains a significant challenge. Herein, the Er[3+] single-doped NaGdTi$_{1.8}$Al$_{0.2}$O$_6$ double perovskite material achieves multicolor luminescence, afterglow, and upconversion emission by responding to several types of excitation ranging from UV to NIR and thermal disturbance. Spectral analysis has revealed that the varying excitation efficiency of the two luminescence centers at various excitation wavelengths leads to a shift in the overall emission color from red to green as the excitation wavelength transitions from 250 nm to 390 nm. Additionally, the energy transfer process between defect levels and Er[3+] leads to multicolor luminescence from green to orange within a temperature range of 217 K to 417 K. These findings offer a facile and unique strategy for designing highly integrated multicolor and multimodal luminescence in a single matrix and promise applications in advanced anti-counterfeiting and information encryption technology.

1. Introduction

Advanced anti-counterfeiting strategies and technologies are invaluable in all aspects of the economic and social sphere, including the security of documents, artworks, and even private data information.[1–3] Multicolor and multimode luminescence materials have received growing attention in anti-counterfeiting and encryption technologies due to their adjustable photon emissions in response to diverse external stimuli, which are generally generated *via* multiple dopant lanthanide ions.[4–6] Nevertheless, the multi-doping strategy still suffers from the complex ionic interactions in the matrix.[7–9] Meanwhile, the co-doping strategy typically requires more luminous ions, which increases the expense and complexity of the synthesis and design of the materials.[10,11] In fact, the

single rare-earth-doped phosphors typically exhibit mono-mode luminescence or limited emitting color.[12] Hence, integrating multicolor and multimodal luminescence into a single matrix with a single lanthanide dopant remains a bottleneck issue.

Considerable efforts have been made to develop single rare-earth-doped phosphors, and various pertinent studies have attracted extensive attention. For instance, Zhang *et al.*[13] reported combining persistent luminescence (PersL), photo-stimulated luminescence, upconversion luminescence (UCL) and photochromism in the Li$_2$CaSiO$_4$:Pr[3+] phosphor. However, the phosphor is equipped with a monochromatic emission color. Zhou *et al.*[14] reported the color-tunable luminescence from white to yellow by exploiting the distinct behaviors of Eu^{2+} ions single-doped in multiple sites of Ca$_6$BaP$_4$O$_{17}$:Eu^{2+}. However, the material showed a limited luminescence mode. Du *et al.*[15] proposed a Sr$_2$YGaO$_5$ phosphor doped with just Sm[3+], exhibiting multimodal and color-changeable luminescence (from violet to rose hermosa), but the phosphor requires constant optical excitation. The current state of research necessitates further investigation to find the appropriate matrix and dopants for effectively integrating multicolor and multimodal luminescence within a single compound doped with a single rare-earth ion.[16–18] The rare-earth-doped

aKey Laboratory of Nonferrous Metal Chemistry and Resources, Utilization of Gansu Province and State Key Laboratory of Applied Organic Chemistry, College of Chemistry and Chemical Engineering, Lanzhou University, Lanzhou 730000, China. E-mail: liuws@lzu.edu.cn
bCollege of Chemistry and Chemical Engineering, Qinghai Normal University, Xining 810016, China
†Electronic supplementary information (ESI) available. See DOI: https://doi.org/10.1039/d4qi00549j

This journal is © the Partner Organisations 2024

Inorg. Chem. Front., 2024, **11**, 4721–4730 | **4721**

perovskite structure has been widely employed in inorganic phosphors due to its remarkable optical characteristics, including sharp emission peaks, multi-level emission, and exceptional photochemical stability.[19–22]

Herein, the effective integration of multicolor and multimodal luminescence in an Er^{3+} single-doped double perovskite $NaGdTi_{1.8}Al_{0.2}O_6$:y%Er^{3+} ($0.1 \leq y \leq 2.0$) (NGTAO:Er^{3+}) was designed and synthesized through high-temperature solid state reactions, free from the use of multiple lanthanide dopants or diverse host matrices. The NGTAO:Er^{3+} samples with various Er^{3+} concentrations exhibit multicolor luminescence (red, orange, yellow and green) and red afterglow when excited by 365 nm ultraviolet (UV) light. In addition, the as-prepared NGTAO:0.1%Er^{3+} successfully integrated excitation-wavelength-dependent color-tunable luminescence (from red to green), external temperature-dependent color variation (from green to orange), and green UCL attributed to Er^{3+} under 980 nm near-infrared (NIR) excitation.[23] Experimental results reveal that two luminescence centers with varying excitation efficiencies at various excitation wavelengths (250–390 nm) are the origins of the tunable excitation-wavelength-dependent multicolor luminescence. Furthermore, the energy transfer process from Er^{3+} to defect levels enables temperature-dependent multicolor luminescence at various temperatures (217–417 K). The designed functional anti-counterfeiting and encryption patterns can be visually read out by using simple tools (cooling–heating stimuli, UV lamps, and a 980 nm NIR laser), based on their multicolor and multimodal emission features. These findings provide a unique strategy for constructing multifunctional optical materials for anti-counterfeiting and encryption applications.

2. Experimental section

Sample preparation

$NaGdTi_{2-x}Al_xO_6$ ($0.1 \leq x \leq 0.5$) and NGTAO:y%Er^{3+} ($0.1 \leq y \leq 2.0$) series of samples were prepared through a high-temperature solid-state reaction process. Na_2CO_3 (99.99%), Gd_2O_3 (99.99%), TiO_2 (99.9%), and Al_2O_3 (99.99%) were purchased from Aladdin and used as the raw materials. A 10% excess of Na_2CO_3 was used to compensate for losses due to volatilization.[19] Typically, a stoichiometric amount of the raw material was mixed and thoroughly ground in an agate mortar for 30 minutes, with an appropriate amount of ethanol as the milling medium. The finely milled powder was placed in a corundum crucible and subjected to annealing in a muffle furnace at 1250 °C for 4 hours. The process occurred in the atmosphere at a heating rate of 5 °C per minute during the ramp stage. Then, the resulting samples were allowed to cool down to room temperature (RT) at a rate of 5 °C min^{-1}, followed by a fine grinding for further testing and characterization. The synthesis of pure NGTAO:y%Er^{3+} ($0.1 \leq y \leq 2.0$) followed the same procedure, with the only change being the addition of Er_2O_3 (Aladdin, 99.99%).

Materials characterization

Powder X-ray diffraction (XRD) patterns of the samples were obtained on a Rigaku D/Max-2400 X-ray diffractometer at RT. Rietveld refinement was carried out using General Structure Analysis System (GSAS) software. An FEI Tecnai F30 transmission electron microscope was used to record the results of energy dispersive spectroscopy (EDS), high-resolution transmission electron microscopy (HRTEM), and microscopic morphology. The XPS tests were carried out on a PHI-5702 instrument and the binding energy was measured using the C 1s peak (284.8 eV) as a reference. The FLS-920T fluorescence spectroradiometer was used to monitor photoluminescence excitation (PLE), photoluminescence (PL), temperature-dependent PL and UCL spectra using a Xe lamp as the excitation source. Additionally, the diffuse reflectance (DR) spectrum was recorded using a PerkinElmer LAMBDA 950. The luminescence decay measurements were conducted at 544 nm and 615 nm under 379 nm and 350 nm excitation *via* an FLS98. The emissions at 544 nm and 615 nm were monitored. The Vienna *Ab initio* Simulation Package (VASP) was employed for the spin-polarized Density Functional Theory (DFT) calculations.

3. Results and discussion

A series of $NaGdTi_{2-x}Al_xO_6$ ($0.1 \leq x \leq 0.5$) and NGTAO:y%Er^{3+} ($0.1 \leq y \leq 2.0$) samples were characterized by XRD, as shown in Fig. S1† and Fig. 1a. All characteristic diffraction peaks were well matched to the standard card PDF#89-3111, revealing the successful formation of the pure phase.[2] As depicted in Fig. 1a, no additional impurity peaks were detected in the NGTAO:Er^{3+} samples due to the small amount of doping ions and the approximately equal radii of Gd^{3+} (CN = 8, r = 1.053 Å) and Er^{3+} (CN = 8, r = 1.004 Å), suggesting the occupation of Er^{3+} dopants in Gd^{3+} sites in accordance with the Hume-Rothery rule.[23] Meanwhile, the diffraction peak of NGTAO shifts in the higher angle direction compared to that of the pure NGTO sample, confirming that the larger Ti^{4+} (CN = 6, r = 0.605 Å) was partially replaced by the smaller Al^{3+} (CN = 6, r = 0.53 Å) (Fig. S1a†).[24] Meanwhile, the subtle replacement of Ti^{4+} by Al^{3+} results in the shrinkage of the crystal lattice.[25] To obtain more information about the structure, the XRD patterns of the sample were calculated by Rietveld refinement of NGTAO:1.0%Er^{3+} (Fig. 1b and Table S1†). The results show good convergence (R_{wp} = 13.62%, R_p = 9.66%, and χ^2 = 0.69) for NGTAO and indicate that the refinement results are reliable, and the phase crystallizes in an orthorhombic perovskite structure based on the *Pnma* (No. 62) space group. The HRTEM reveals the single-crystalline nature of the individual particles, with a d-spacing of 2.67 Å (Fig. S1b†), corresponding to the lattice spacing along the [002] direction of NGTAO. Fig. 1c displays the crystal structure of the NGTAO matrix. Eight oxygen ions coordinate with the sites occupied by Na^+/Gd^{3+} ions, while six oxygen ions coordinate with the sites occupied by Al^{3+}/Ti^{4+} ions. This exacerbates the tilting of the $[TiO_6]$/$[AlO_6]$ octahedra.[19] Additionally, the EDS images of NGTAO:

4722 | *Inorg. Chem. Front.*, 2024, **11**, 4721–4730

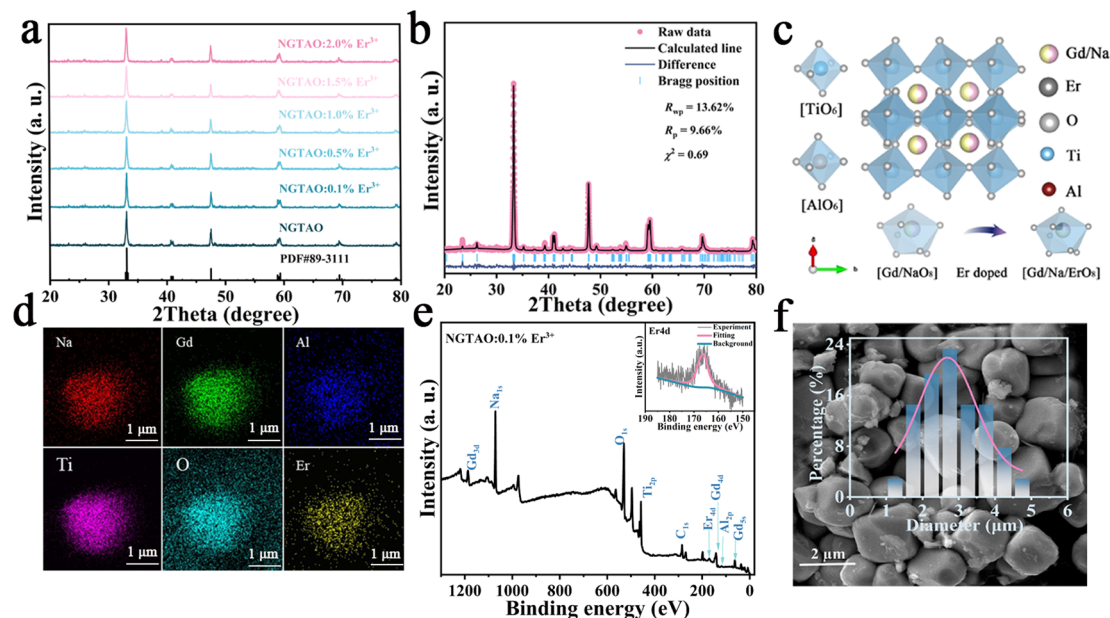This journal is © the Partner Organisations 2024

Fig. 1 Morphological and structural characterization: (a) XRD patterns with different Er^{3+} concentrations. (b) Rietveld refinement of the powder XRD profile. Inset: calculated parameters. (c) The crystal structure of NGTAO. (d) The mapping images of the elements Na, Gd, Al, Ti, and O, respectively. (e) The XPS survey spectrum of NGTAO:0.1%Er^{3+}. Inset: XPS spectrum of Er 4d. (f) SEM of NGTAO:$y$$Er^{3+}$.

Er^{3+} confirm the presence of Na, Gd, Ti, Al, O and Er elements, demonstrating that all of the constituent elements are uniformly distributed within the as-prepared NGTAO:Er^{3+} single particle (Fig. 1d and Fig. S1c†). The XPS spectra of NGTAO:0.1% Er^{3+} further demonstrate that the prepared compounds are composed of Na, Gd, Ti, Al, O and Er (Fig. 1e and inset).[26] A representative SEM micrograph of the NGTAO:1.0% Er^{3+} sample reveals a relatively regular morphology with an average size of 1–5 μm (Fig. 1f and inset).

We next investigated the multicolor and multimode luminescence properties of NGTAO and NGTAO:Er^{3+}. The normalized PLE and PL spectra of the as-obtained NGTAO:Er^{3+} are given in Fig. 2a. Under 350 nm excitation, the PL spectrum displays a wide emission range between 570 nm and 660 nm centered at 615 nm, which can be ascribed to the existence of oxygen-related defects, *i.e.* interstitial oxygen in the matrix.[27–30] By monitoring the emission spectra at 615 nm, the observed PLE spectrum reveals a band peak at 350 nm, which can be attributed to the host absorption band. The shoulder band PLE spectra were monitored at 544 nm, ranging from 355 nm to 395 nm. This range corresponds to the characteristic excitation of NGTAO:Er^{3+}, originating from the $^{4}I_{15/2} \rightarrow ^{4}G_{11/2}$ and $^{4}I_{15/2} \rightarrow ^{2}H_{9/2}$ transitions of Er^{3+}.[26] Importantly, the excitation regions of red and green emissions have a partial spectral overlap in the 360–395 nm range, indicating that tunable color in the red-green range of NGTAO:Er^{3+} can be obtained through simultaneously pumping different ratios of green/red emission by adjusting the excitation wavelength. Microstructures such as defects also play an important role in intrinsic luminescence.[2] To investigate the regulating effect of Al^{3+} on the PL of $NGT_{2-x}A_{x}O_{6}$, the relationship between the PL intensity of the

$NGT_{2-x}A_{x}O_{6}$ samples at different concentrations of Al^{3+} ($x = 0$, 0.1, 0.2, 0.3, 0.4, and 0.5) is shown in Fig. 2b. Interestingly, the heterovalent substitution of Al^{3+} for Ti^{4+} does not affect the positions of the red emission peaks, and the PL intensity at 615 nm in NGTAO is enhanced significantly after Al^{3+} is added. The addition of a small amount of Al^{3+} increases the asymmetry of the crystal lattice,[19] leading to lattice shrinkage and ultimately enhancing the effectiveness of the energy transfer. This results in an increased luminescence intensity.[25] The maximum PL intensity is observed when the Al^{3+} ion content is 0.2. As the content of Al^{3+} increases further, the distance between defects decreases (Fig. 1c), leading to the occurrence of the so-called concentration quenching effect (Fig. 2b).[24,25]

According to the aforementioned results, red emissions are found in NGTAO under UV light. To investigate the multicolor luminescence performance under the same excitation source, the emissions of NGTAO:y%Er^{3+} ($0.0 \leq y \leq 2.0$) are measured upon excitation at 365 nm and shown in Fig. 2c. As the concentration of Er^{3+} dopant increases, the green emission is enhanced and the red emission shows negligible change. At low concentrations of dopant, we observe that the emission at 615 nm primarily dominates the PL spectrum. The green emission at 544 nm becomes more noticeable and begins to dominate the PL as the concentration of Er^{3+} rises. The trend in the integrated intensity ratio ($I_{544\ nm}/I_{615\ nm}$) incrementally indicates that the relative contribution of emission peaks centered at 544 nm increases as the Er^{3+} dopant concentration increases from 0.0% to 2.0% (Fig. 2d), leading to a dopant concentration-dependent color change from red to green.

To get detailed information about the species responsible for luminescence in the NGTAO:Er^{3+} samples, the fluorescence
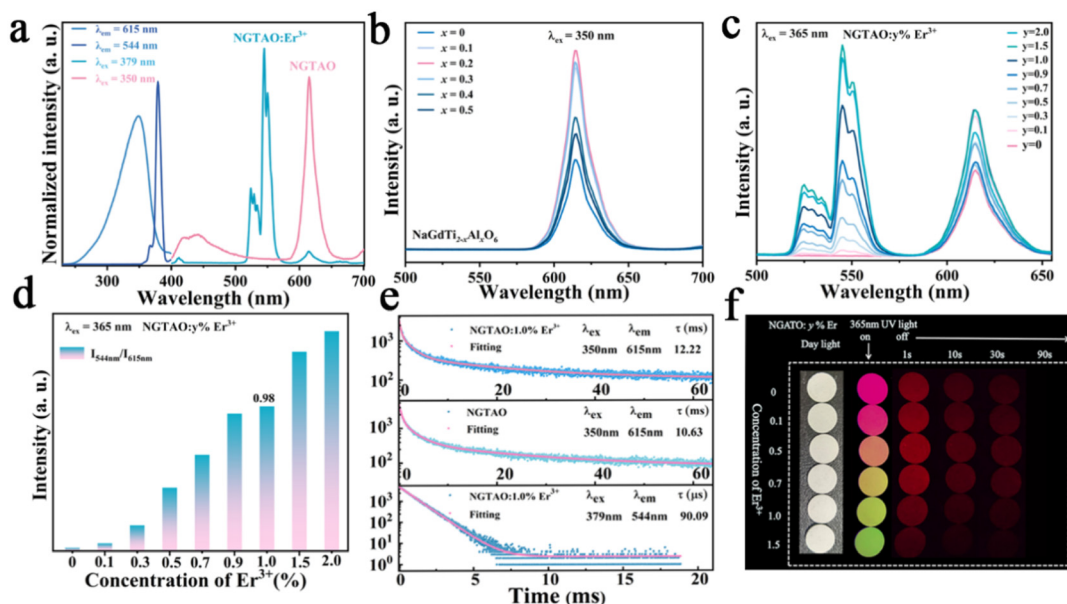
This journal is © the Partner Organisations 2024

Inorg. Chem. Front., 2024, **11**, 4721–4730 | **4723**

Fig. 2 (a) PLE and PL spectra of NGTAO:1.0%Er³⁺. (b) PL spectra of NGT₂₋ₓAₓO₆ under 350 nm excitation. (c) PL spectra and (d) integrated intensity ratio ($I_{544\ nm}/I_{615\ nm}$) of NGTAO:y%Er³⁺ (0.1 ≤ y ≤ 2.0) under 365 nm excitation. (e) PL lifetime curves of NGTAO and NGTAO:y%Er³⁺ measured under 350 nm and 379 nm excitation, respectively. (f) Photos of the concentration-dependent color of NGTAO:y%Er³⁺ (0.1 ≤ y ≤ 2.0).

decay curves corresponding to emissions from the samples were recorded. The decay curves were fitted by using the following equation:[31]

$$I(t) = A_0 + \sum_{i=1}^{4} A_i \exp(-t/\tau_i)$$

where $I(t)$ represents the intensity at time t, t stands for the time, A_0 and A_i are constants, and τ_i is the characteristic lifetime. This lifetime is further used to calculate the average decay time via the following formula:[32]

$$\tau = \sum_{i=1}^{4} A_i \tau_i^2 \Big/ \sum_{i=1}^{4} A_i \tau_i$$

Tables S2 and S3† list the derived average decay times and fitting parameters, respectively. The calculated results are presented in Fig. S2a and S2b.† As the concentration of Er³⁺ increases from 0.1% to 2.0%, the average decay durations for green emissions decrease (Fig. S2a†), while the red emissions exhibit an opposite trend (Fig. S2b†). This suggests enhanced non-radiative energy transfer at the higher doping levels.[29] In contrast to the lifetime of green emission at 544 nm (90.09 μs), the red emission at 615 nm shows a significantly longer lifetime of 13.58 ms, as seen in Fig. 2e. This observation confirms the energy transfer from Er³⁺ to defect levels.[26] In addition, the decay curves of red emission exhibit a long temporal tail, which correlates to the red afterglow.[31,32] The photos (Fig. 2f) and CIE chromaticity coordinates (Fig. S2c†) of the NGTAO: Er³⁺ samples clearly show that the observed emission color shifts from red to orange, yellow and green progressively, with the concentration of Er³⁺ increasing from 0.0% to 2.0%. When

the 365 nm irradiation is removed, the colorful luminescence disappears immediately due to the green luminescence from Er³⁺ vanishing, and the samples only exhibit the red afterglow (Fig. 2f). As a result, a series of multicolor-emitting phosphors were obtained through Er³⁺ doping concentration modulation.

Further excitation-wavelength-dependent PL and temperature-dependent PL measurements of the representative NGTAO:1.0%Er³⁺ sample were also carried out to obtain more insight into its luminescence properties. As expected, the emission colors of the NGTAO:1.0%Er³⁺ sample exhibit an obvious excitation-wavelength-dependent PL, which is obtained by integrating the green PL of Er³⁺ and the red emission of defect levels, as illustrated in Fig. 3a. Fig. 3b depicts the integrated luminescence intensities of $I_{544\ nm}$ and $I_{615\ nm}$ with the excitation wavelength range from 250 nm to 400 nm. The PL intensity of the red emission reaches a maximum at 350 nm and then decreases with the continuous increase of excitation wavelength, while the green emission is produced at 355 nm and decreases rapidly after 380 nm. The corresponding chromaticity coordinates of the wavelength-dependent PL were calculated and are shown in Fig. 3c. The PL color switched from red to green when the excitation wavelength increased from 250 nm to 390 nm, due to the shift in the relative intensity of the two different wavelengths at 615 nm and 544 nm in the PL spectrum. This shift allows for precise control over the emission color by adjusting the excitation wavelength. Fig. 3d shows the temperature-dependent luminescence behavior under 365 nm excitation of the NGTAO:1.0% Er³⁺ sample. The trend of temperature-dependent PL intensity in the NGTAO:1.0%Er³⁺ samples at various temperatures (217–417 K) is shown in Fig. 3e. It can be observed that as the
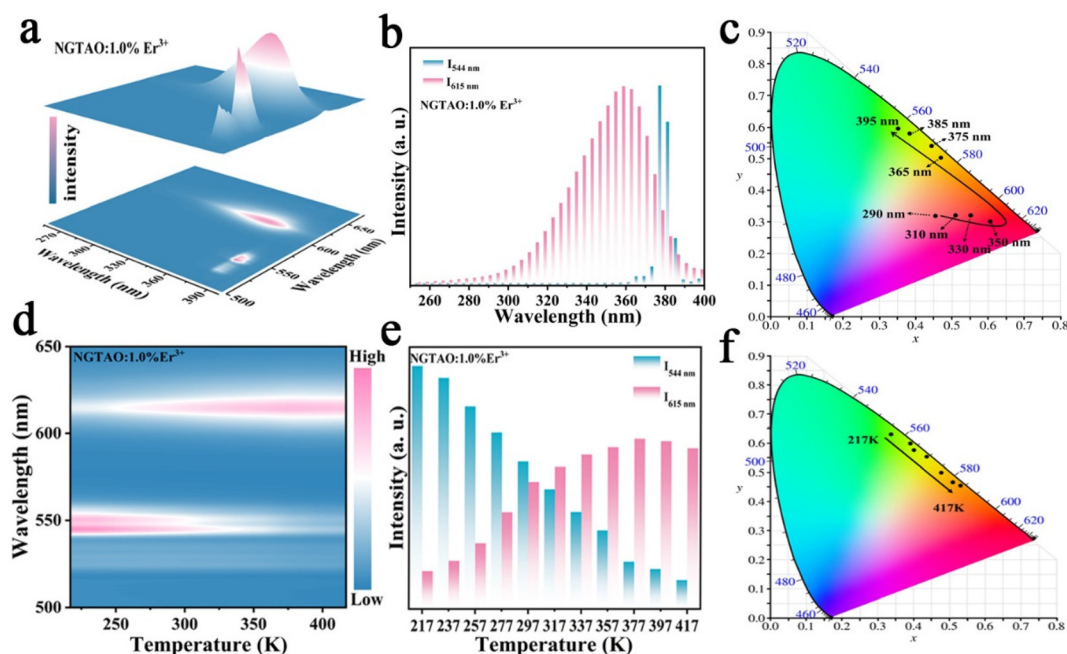
4724 | *Inorg. Chem. Front.*, 2024, **11**, 4721–4730

This journal is © the Partner Organisations 2024

Fig. 3 (a) 3D PL spectra and (b) the integrated intensity of $I_{544 \text{ nm}}$ and $I_{615 \text{ nm}}$ from NGTAO:1.0%Er^{3+} under 250–400 nm UV excitation. (c) CIE 1931 coordinates of the wavelength-dependent color of NGTAO:1.0%Er^{3+}. (d) The temperature-dependent PL spectra and (e) the integrated luminescence intensities of $I_{544 \text{ nm}}$ and $I_{615 \text{ nm}}$ from NGTAO:1.0%Er^{3+} at different temperatures under 365 nm excitation. (f) CIE coordinates of the temperature-dependent color of NGTAO:1.0%Er^{3+}.

temperature increased from 217 K to 377 K, the red emission intensity increased while the intensity of the green emission decreased (Fig. 3e). The energy transfer from emission centers (Er^{3+}) to defect levels is thus confirmed again. In addition, the following slight decrease in red emission is observed as the temperature increases from 377 K to 417 K, which is attributed to the temperature quenching effect.[33,34] The results indicate that NGTAO exhibits proficient intrinsic luminescence and thermal stability, making it a highly promising contender for a wide range of potential applications. The corresponding chromaticity coordinates of the temperature-dependent PL were calculated and are shown in Fig. 3f, showing that the adjustable emission colors, ranging from green to orange, were achieved at different temperatures (217–417 K). Based on the study above, the color outputs of the developed NGTAO: Er^{3+} samples can be easily adjusted by controlling dopant concentrations, excitation wavelengths, and external temperatures.

To further investigate the UCL properties of NGTAO:Er^{3+}, the green-emitting UCL measurements of the samples were carried out and the results are displayed in Fig. 4. The UCL spectra of NGTAO:y%Er^{3+} ($0.1 \leq y \leq 2.0$) present similar shapes and positions compared to those observed in the PL spectra (Fig. 4a). According to the experimental data, the $^2\text{H}_{11/2} \rightarrow {}^4\text{I}_{15/2}$ and $^4\text{S}_{3/2} \rightarrow {}^4\text{I}_{15/2}$ transitions of Er^{3+} are the origins of the emissions at 534 nm and 544 nm, respectively.[35] The emission intensity of the two peaks rises gradually as the concentration of Er^{3+} increases and reaches the maximum at y = 1.5. As expected, the UCL intensity increases as the pump density increases from 0.5 to 2.0 mW cm^{-2}, resulting in a

series of progressively brighter green visible patterns (Fig. 4b). The relationship between UCL emission intensity and pump density of the NIR laser is explored according to the following equation: $I \propto P^n$. Here, I refers to the UCL emission intensity, the pump density is represented by P, while n denotes the number of photons required in the upconversion process.[36] The fitted slopes of the two main emissions are both close to 2, confirming the involvement of a two-photon absorption process in the UCL (Fig. 4c).[35] Possible UCL mechanisms are depicted in Fig. 4d. Under 980 nm laser irradiation, the green-emitting levels $^2\text{H}_{11/2}$ and $^4\text{S}_{3/2}$ were populated through the $^4\text{I}_{15/2}$–$^4\text{I}_{11/2}$ ground state absorption (GSA) and the $^4\text{I}_{11/2}$–$^4\text{F}_{7/2}$ excited state absorption (ESA), followed by successive non-radiative relaxation from $^4\text{F}_{7/2}$ to $^2\text{H}_{11/2}$ and $^4\text{S}_{3/2}$.[36] The electrons finally return to the $^4\text{I}_{15/2}$ level with intense UC emission at 534 nm and 544 nm, respectively.[35]

Fig. 5a and the inset show the luminescence decay curves of the red emission in NGTAO:y%Er^{3+} ($0 \leq y \leq 2.0$) phosphors after being excited by 365 nm radiation for 5 min. The samples exhibit noticeable red afterglow for up to 200 s. It was observed that the PersL duration of the NGTAO sample was longer than that of the NGTAO:Er^{3+} samples. This suggests that the presence of Er^{3+} reduces the trapping centers compared to the NGTAO sample, resulting in a decrease in the PersL duration after doping with Er^{3+}.[36] The afterglow curve peaks corresponding to thermal energies indicate traps at different depths responsible for PersL.[37] To further reveal more information about the traps, a thermoluminescence (TL) study was conducted. Generally, Urbach's empirical formula
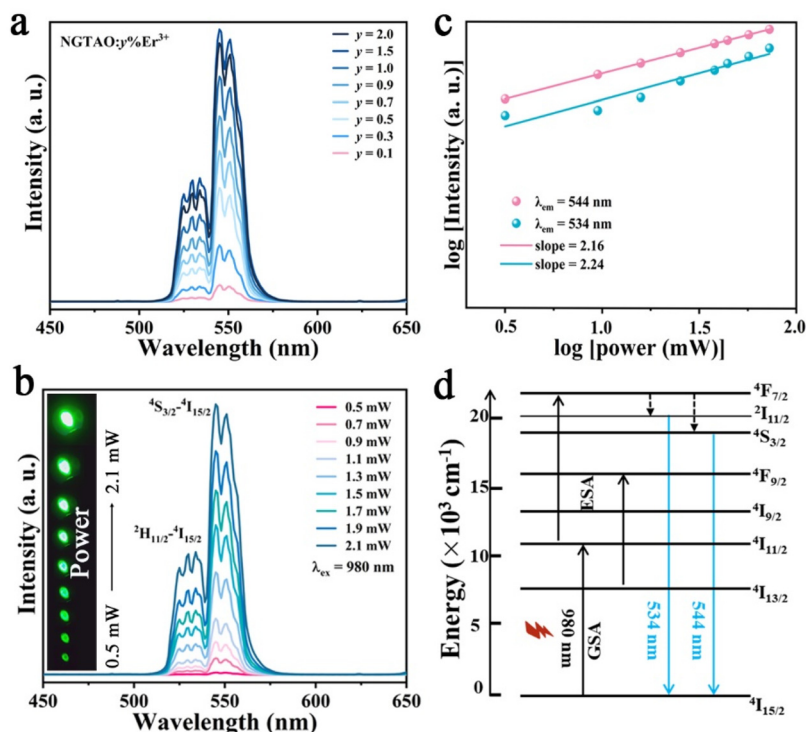
This journal is © the Partner Organisations 2024

Inorg. Chem. Front., 2024, **11**, 4721–4730 | **4725**

Fig. 4 Dependence of the UCL spectra on the 980 nm laser power density. (a) PL spectra of NGTAO:y%Er^{3+} (0.1 ≤ y ≤ 2.0) under 379 nm excitation. (b) UCL spectra of NGTAO:1.0%Er^{3+} at different pump powers and (c) double logarithmic plots of excitation power *versus* UCL intensity of Er^{3+} at 534 nm and 544 nm for NGTAO:1.0%Er^{3+}. (d) Energy level diagram and corresponding possible UC processes of NGTAO:Er^{3+}.

$E_{trap} = T_m/500$ can be used to calculate trap depth.[37] Here, T_m represents the temperature of the peak position of the TL curve, and E denotes the trap depth. The TL curves of the NGTO, NGTAO, and NGTAO:1.0%Er^{3+} samples exhibit peaks at 330 K, 354 K, and 335 K after irradiation at 365 nm for 5 min, as shown in Fig. 5b. The corresponding trap depths are 0.66 eV, 0.70 eV, and 0.67 eV, respectively. For all three samples, the trap depths are smaller than 0.8, which is suitable for the PersL luminescence generation at RT.[38] We observed that the presence of Al^{3+} caused the peak of the TL curve to shift towards higher temperatures, from 330 K to 354 K. On the other hand, the presence of Er^{3+} caused the peak to shift towards lower temperatures, from 354 K to 335 K. This implies that the addition of Al^{3+} increased the depth of the electron traps, while the addition of Er^{3+} had the opposite effect.[26,35] The above results are consistent with the trend of the afterglow phenomenon of the corresponding compounds in Fig. 5a. A series of TL decay curves for various charge durations of NGTAO:1.0%Er^{3+} samples were obtained and are depicted in Fig. 5c and the corresponding trap depths were calculated as shown in Fig. 5d. The ideal continuous trap depth distribution from 0.66 eV to 0.69 eV ensures that NGTAO:1.0%Er^{3+} can produce long lifetime trapping carriers below the band-edge, and then yield afterglow emission.[39] According to the wavelength-resolved TL spectra of NGTAO:1%Er^{3+} in Fig. 5e, the profile and maximum wavelength (~615 nm) of the TL emission are in line with the PL spectra of the host in Fig. 2a,

which further demonstrates that the PersL originated from matrix defect energy levels.[39]

The luminescence performance is directly related to the properties of the matrix. To investigate the electronic energy band structure in detail, the optical band gap (E_g) measurements and evaluation were carried out. The diffuse reflectance of the samples was measured and converted using the Kubelka–Munk function:[40]

$$F(R) = (1 - R)^2/2R$$

and the $[F(R_\infty)h\nu]^2$ versus $h\nu$ plots were made in accordance with the following function:[40]

$$F(R_\infty)h\nu = A(h\nu - E_g)^n$$

where R, $h\nu$, and A are the reflection coefficient, photon energy, and a constant, respectively, and $n = 1/2$ since NGTAO is a direct semiconductor.[41] The intercept of a fitted straight line was used to calculate the band gap energy for each sample (Fig. S3a and S3b†). Fig. 5f shows that the fitting results of NGTO, NGTAO, and NGTAO:1.0%Er^{3+} give optical band gaps of 3.34 eV, 3.28 eV, and 3.21 eV, respectively. The partial and total densities of states (DOS) of NGTO and NGTAO were calculated by DFT. The data are shown in Fig. 5g and h, while the computational details are shown in the ESI.† It can be observed that NGTAO possesses a direct band gap, with the maximum of the valence band (VB) and the minimum of the conduction band
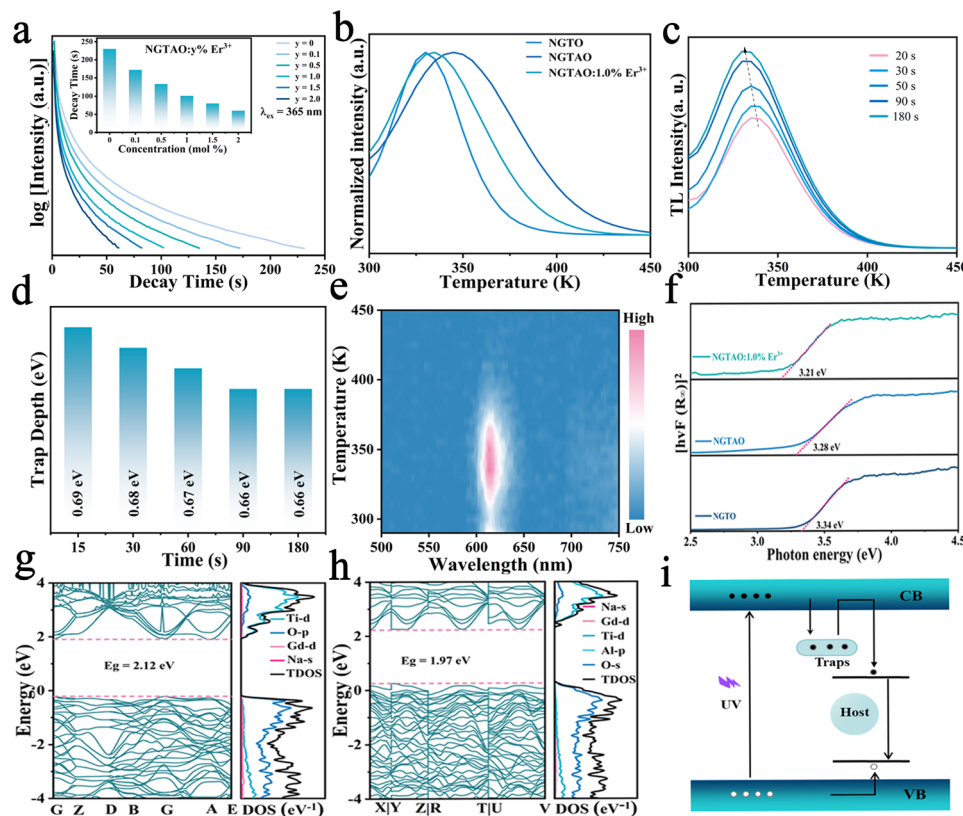
4726 | *Inorg. Chem. Front.*, 2024, **11**, 4721–4730

This journal is © the Partner Organisations 2024

Fig. 5 (a) Afterglow decay curves of NGTAO:y%Er^{3+} (0.1 ≤ y ≤ 2.0) after 365 nm UV irradiation. (b) TSL curve of the NGTO, NGTAO, and NGTAO:1.0%Er^{3+} phosphors after 365 nm excitation for 5 minutes. (c) TSL curve of the NGTAO:1.0%Er^{3+} phosphor at different time intervals after 5 minutes of excitation under 365 nm UV. (d) Trap depth distribution in NGTAO:1.0%Er^{3+}. (e) Contour plot of the TL curve of the NGTAO:1.0%Er^{3+} after 365 nm illumination. (f) The band gap values of NGTO, NGTAO, and NGTAO:1.0%Er^{3+}. Calculated electronic band structures and DOS of (g) NGTO and (h) NGTAO. (i) An energy diagram with a proposed plausible mechanism for the afterglow and PL mechanism.

(CB) situated at the same location on G.[42] The predicted band gap for NGTAO was about 1.97 eV. This value was lower than the experimental value of roughly 3.34 eV, which should be attributed to the acknowledged PBE functional errors.[31] The VB is mainly dominated by the O$_{2p}$ orbitals and the CB is composed mostly of the Ti$_{3d}$ orbitals, as shown by the total and partial DOS of the NGTAO.[43] The above results demonstrate that the heterovalent substitution of the Al^{3+} ions for Ti^{4+} ions reduces the band gap and introduces trapped energy levels, increasing the conducting carriers and the absorption channel, simultaneously.[19,44] This result is in accordance with the experimental results (Fig. S3a and S3b†). A theoretical model of the luminescence mechanism is clarified and schematically represented in Fig. 5i based on the analysis presented above. Under UV irradiation, the electrons in the VB are promoted to the CB. The excited electrons are then captured by electron traps.[32] Some of the excited electrons relax through the nonradiative transition to the defect levels, leading to red PL emission. After the cessation of UV irradiation, the electrons stored in the traps escape into the CB by thermal vibration at RT. Subsequently, they are gradually released to the defect levels, resulting in afterglow luminescence.

The multicolored and multimodal luminescence properties of NGTAO:Er^{3+} phosphors offer significant potential for anti-

counterfeiting and information encryption technologies. We designed a 3D printed polylactic acid device (resembling an apple tree, see Fig. 6a) based on the distinction of PL color, UCL, and different afterglow duration, filled with typical NGTAO:y%Er^{3+} (where y = 0.1, 0.5, 0.7, 1.0, and 1.5) samples. Under various wavelengths of irradiation in the range of 310–380 nm, the output color of the apple tree's photoluminescence pattern is extremely sensitive to the excitation wavelength. When stimulated with a 980 nm NIR laser, a bright green UCL can be achieved. Notably, under 365 nm UV lamp irradiation, the NGTAO:Er^{3+} phosphors exhibit excellent multicolor PL and a red afterglow. The green "tree outline" pattern is visible with four apples (red, orange, yellow, and yellowish-green) simultaneously. However, it shows a red afterglow immediately after the lamp is turned off, and their brightness gradually decreases over time. The tree outline disappeared after 10 s, and only the "red apples" pattern remains visible. When the pattern was cooled, the brightness of the "apples" decreased. While the pattern was being heated, the "apple tree" emitted a light red emission. Furthermore, multicolor and multimodal luminescence imaging of the NGTAO:Er^{3+} phosphors were also employed for information encryption (Fig. 6b). The NGTAO:y%Er^{3+} (where y = 0.1, 0.5, 0.7, and 1.0) patterns contain concealed correct information. Under the
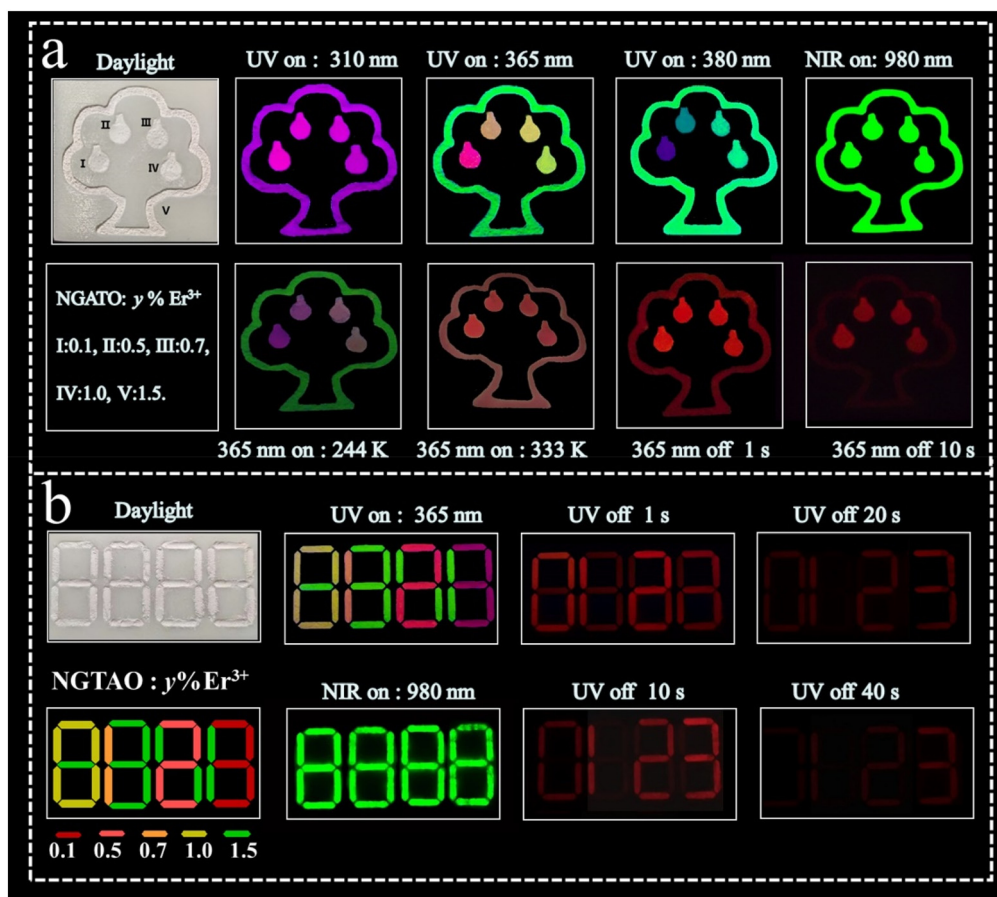
This journal is © the Partner Organisations 2024

Inorg. Chem. Front., 2024, **11**, 4721–4730 | **4727**

Fig. 6 Applications of multicolor and multimodal luminescence features in (a) anticounterfeiting and (b) information encryption based on NGTAO: Er^{3+} phosphors.

stimulation of a 980 nm NIR laser, all the interference information "green 8888" becomes visible. Under the 365 nm UV lamp, the interference information "multicolored 8888" is visible, but when the UV lamp is switched off, the correct information "red 0123" becomes visible within 20 s. As time elapses, only the correct information pattern "3" is visible and displayed after 40 s. This mode enriches the encryption dimension and improves the level of confidentiality. Consequently, the developed NGTAO:Er^{3+} phosphors provide exceptional potential for use in anticounterfeiting and encryption in terms of multicolor and multimodal luminescence features.

4. Conclusion

In summary, we present a design principle for integrating multicolor and multimodal (PL, UCL, PersL) luminescence properties based on a single platform *via* an Er^{3+} single rare-earth doped double perovskite. We have demonstrated that substituting Ti^{4+} with Al^{3+} ions in NGTAO can effectively enhance the matrix emission. Parallelly, by multiplexing the emission from the host and dopant effectively, distinct emissions and multimodal luminescence properties have been achieved, avoiding

the employment of multiple lanthanide ions or matrices. Thus, the tunable PL emissions can range from red to green and can be controlled simply by adjusting the doping concentration, excitation wavelength, and ambient temperature. The NGTAO:$y\%Er^{3+}$ ($0.1 \leq y \leq 2.0$) phosphors were successfully utilized to fabricate anti-counterfeiting and encrypted information patterns with high-level security, based on their excellent optical tunability. Finally, our study presents a facile yet efficient approach to achieve adjustable multicolor and multimode luminescence by integrating the luminescence features originating from defect levels and rare earth emission centers. Our strategy might inspire new ideas for developing optical tuning and anti-counterfeiting technology.

Conflicts of interest

The authors declare no conflict of interest.

Acknowledgements

References

1 J. Bai, Z. Shi and X. Jiang, "Acrostic" Encryption: Stress-Manipulation on Information Display, *Adv. Funct. Mater.*, 2023, **33**(31), 2301797.

2 X. Zhou, L. Ning, J. Qi, Y. Zha, P. Xiong and Z. Xia, Interplay of defect levels and rare earth emission centers in multimode luminescent phosphors, *Nat. Commun.*, 2022, **13**, 7589.

3 K. Huang, N. Le, J. Wang, L. Huang, L. Zeng, W. Xu, Z. Li, Y. Li and G. Han, Designing Next Generation of Persistent Luminescence: Recent Advances in Uniform Persistent Luminescence Nanoparticles, *Adv. Mater.*, 2022, **34**(14), 2107962.

4 X. Zhang, X. Hou, J. Gao, Z. Wang, X. Zhao, C. Xu and D. Gao, Colour evolution of dynamic persistent luminescence of $Zn_3Ga_2Ge_2O_{10}$:Cr^{3+}, Mn^{2+} phosphors for advanced anti-counterfeiting, *J. Mater. Chem. C*, 2023, **11**, 16631–16637.

5 M. Deng, Q. Liu, Y. Zhang, C. Wang, X. Guo, Z. Zhou and X. Xu, Novel Co-Doped Y_2GeO_5:Pr^{3+}, Tb^{3+}: Deep Trap Level Formation and Analog Binary Optical Storage with Submicron Information Points, *Adv. Opt. Mater.*, 2021, **9**(10), 2002090.

6 H. Sun, X. Li, Y. Zhu, X. Wang, Q. Zhang and X. Hao, Achieving multicolor emission readout and tunable photoswitching via multiplexing of dual lanthanides in ferroelectric oxides, *J. Mater. Chem. C*, 2019, **7**, 5782–5791.

7 G. Gao, D. Busko, N. Katumo, R. Joseph, E. Madirov, A. Turshatov, I. A. Howard and B. S. Richards, Ratiometric Luminescent Thermometry with Excellent Sensitivity over a Broad Temperature Range Utilizing Thermally–Assisted and Multiphoton Upconversion in Triply–Doped La_2O_3: Yb^{3+}/Er^{3+}/Nd^{3+}, *Adv. Opt. Mater.*, 2020, **9**(5), 2001901.

8 L. Liang, J. Chen, K. Shao, X. Qin, Z. Pan and X. Liu, Controlling persistent luminescence in nanocrystalline phosphors, *Nat. Mater.*, 2023, **22**, 289–304.

9 Q. Wu, Q. Zhang, W. Li, L. Luo and P. Du, Tailoring of visible light driven photocatalytic activities of Bi_2MoO_6 flower-like microspheres via synergistic effect of doping and surface Plasmon resonance, *Chem. Eng. J.*, 2023, **475**, 146192.

10 X. Zhang, H. Suo, Y. Wang, B. Chen, W. Zheng, Q. Wang, Y. Wang, Z. Zeng, S. Tsang, D. Tu and F. Wang, Systematic Tuning of Persistent Luminescence in a Quaternary Wurtzite Crystal Through Synergistic Defect Engineering, *Laser Photonics Rev.*, 2023, **17**(9), 230013.

11 J. Zhang, C. Pan, Y. Zhu, L. Zhao, H. He, X. Liu and J. Qiu, Achieving Thermo–Mechano–Opto–Responsive Bitemporal Colorful Luminescence via Multiplexing of Dual Lanthanides in Piezoelectric Particles and its

12 H. Lv, L. Luo, W. Li and P. Du, Manipulating Upconversion Emission and Thermochromic Properties of Ho^{3+}/Yb^{3+}-Codoped $Al_2Mo_3O_{12}$ Microparticles by Negative Lattice Expansion for Multimode Visual Optical Thermometry, *Inorg. Chem.*, 2022, **61**, 11442–11453.

13 Y. Zhang, X. Shan, X. Lv, D. Chen, S. Miao, W. Wang and Y. Liang, Multimodal luminescence in Pr^{3+} single-doped Li_2CaSiO_4 phosphor for optical information storage and anti-counterfeiting applications, *Chem. Eng. J.*, 2023, **474**, 145886.

14 R. Zhou, C. Liu, L. Lin, Y. Huang and H. Liang, Multi-site occupancies of Eu^{2+} in $Ca_6BaP_4O_{17}$ and their potential optical thermometric applications, *Chem. Eng. J.*, 2019, **69**, 376–385.

15 J. Du, S. Lyu, P. Wang, T. Wang and H. Lin, Multimode-responsive luminescence smart platform by single-Sm^{3+}-doped phosphors, *Adv. Opt. Mater.*, 2023, **11**(12), 2300359.

16 D. Gao, K. Ma, P. Wang, X. Zhang, Q. Pang, H. Xin, Z. Zhang and H. Jiao, Tuning multicolour emission of Zn_2GeO_4:Mn phosphors by Li^+ doping for information encryption and anti-counterfeiting applications, *Dalton Trans.*, 2022, **51**(2), 553–561.

17 T. Zheng, M. Runowski, J. Xue, L. Luo, U. R. Rodríguez-Mendoza, V. Lavín, I. R. Martín, P. Rodríguez-Hernández, A. Muñoz and P. Du, Giant Pressure-Induced Spectral Shift in Cyan-Emitting Eu^{2+}-Activated $Sr_8Si_4O_{12}Cl_8$ Microspheres for Ultrasensitive Visual Manometry, *Adv. Funct. Mater.*, 2023, **33**, 2214663.

18 D. Gao, Q. Kuang, F. Gao, H. Xin, S. Yun and Y. Wang, Achieving opto-responsive multimode luminescence in $Zn_{1+x}Ga_{2-2x}Ge_xO_4$: Mn persistent phosphors for advanced anti-counterfeiting and information encryption, *Mater. Today Phys.*, 2022, **27**, 100765.

19 Y. Inaguma, T. Tsuchiya and T. Katsumata, Systematic study of photoluminescence upon band gap excitation in perovskite-type titanates $R_{1/2}Na_{1/2}TiO_3$:Pr (R=La, Gd, Lu, and Y), *J. Solid State Chem.*, 2007, **180**(5), 1678–1685.

20 P. Zhang, W. Xie, Z. Lin, X. Huang, Y. Yang and W. Liu, Opto–Mechano–Thermo–Sensitive Allochroic Luminescence Based on Solution–Grown Halide Double Perovskite Crystal, *Laser Photonics Rev.*, 2023, **17**(12), 230026.

21 W. Yin, B. Weng, J. Ge, Q. Sun, Z. Li and Y. Yan, Oxide perovskites, double perovskites and derivatives for electrocatalysis, photocatalysis, and photovoltaics, *Energy Environ. Sci.*, 2019, **12**(2), 442–462.

22 T. Zheng, L. Luo, P. Du, S. Lis, U. R. Rodríguez-Mendoza, V. Lavín and M. Runowski, Highly-efficient double perovskite Mn^{4+}-activated Gd_2ZnTiO_6 phosphors: A bifunctional optical sensing platform for luminescence thermometry and manometry, *Chem. Eng. J.*, 2022, **446**, 136839.

23 X. Cheng, Y. Pan, Z. Yuan, X. Wang, W. Su, L. Yin, X. Xie and L. Huang, Er^{3+} sensitized photon upconversion nanocrystals, *Adv. Funct. Mater.*, 2018, **28**(22), 180020.

24 W. Hume-Rothery, Some notes on the structures of alloys of iron, *Contemp. Phys.*, 1964, **5**(5), 321–347.

25 Y. Yang, Y. Shi, J. Duan, K. Lu, G. Cheng, Y. Zhao, Z. Huang, P. Li, N. Wei, X. Zhu, J. Qi and T. Lu, Photoluminescence enhancement of $Gd_2Zr_2O_7$:Eu^{3+} red phosphor sensitized by co-doped Al^{3+} ions, *Ceram. Int.*, 2021, **47**, 13071–13077.

26 H. Liu, X. Zhu, L. Nie, L. Guo, C. Jiang, G. Wang, W. Huang, L. Hou, T. Hu, A. N. Yakovlev, X. Yu and T. Wang, Multimode-Responsive Luminescence of Er^{3+} Single-Activated CaF_2 Phosphor for Advanced Information Encryption, *Inorg. Chem.*, 2023, **62**(40), 16485–16492.

27 J. Jia, X. Gao and G. Zou, Alkaline-Earth-Metal-Ions Blending Enhanced Self-Activated and Bi^{3+}-Activated Mechanoluminescence from $Ca_{1-x}Ba_xZnOS$, *Adv. Funct. Mater.*, 2022, **32**, 2207881.

28 N. Zhang, B. Tian, Z. Wang, A. T. Smith, Z. Ma, Z. Xue and L. Sun, Intense Mechanoluminescence in Undoped $LiGa_5O_8$ with Persistent and Recoverable Behaviors, *Adv. Opt. Mater.*, 2021, **9**, 2100137.

29 J. Zhang, T. Zhang, Z. Qiu, S. Liu, J. Zhang, W. Zhou, L. Yu and S. Lian, Fine-Tunable Self-Activated Luminescence in Apatite-Type $(Ba,Sr)_5(PO_4)_3Br$ and the Defect Process, *Inorg. Chem.*, 2018, **57**(19), 12354–12363.

30 W. Lü, X. Kang, Z. Zhu, Q. Pan, F. Zhou and H. Wang, A novel self-activated near-infrared luminescence of $BaLaMgTaO_6$ phosphor, *J. Mol. Struct.*, 2024, **1298**, 137082.

31 Y. Yang, P. Zhan, W. Xie, Z. Lin, X. Miao, S. Li, H. Wang and W. Liu, Time-dependent multicolor evolution of photoluminescence and afterglow in lanthanide-doped gallate, *Chem. Eng. J.*, 2023, **476**, 14648.

32 L. Li, T. Li, Y. Hu, C. Cai, Y. Li, X. Zhang, B. Liang, Y. Yang and J. Qiu, Mechanism of the trivalent lanthanides' persistent luminescence in wide bandgap materials, *Light: Sci. Appl.*, 2022, **11**, 51.

33 J. Wang, B. Liu, W. Chen, Q. Qiang, L. Peng, T. Han, T. Zeng, Z. Zhou, Z. Yang and Y. A. Nikolaevich, Variable temperature persistent luminescence properties of phosphors with continuous traps, *J. Lumin.*, 2022, **243**, 118644.

34 Y. Wei, Y. Pan, E. Zhou, Z. Yuan, H. Song, Y. Wang, J. Zhou, J. Rui, M. Xu, L. Ning, Z. Liu, H. Wang, X. Xie, X. Tang, H. Su, X. Xing and L. Huang, Frenkel Defect-modulated Anti-thermal Quenching Luminescence in Lanthanide-doped $Sc_2(WO4)_3$, *Angew. Chem., Int. Ed.*, 2023, **62**(27), e202303482.

35 W. Liu, Y. Zhang, X. Kong, E. Y. B. Pun and H. Lin, Excitation Mechanism Rearrangement in Yb^{3+}-Introduced La_2O_2S: Er^{3+}/Polyacrylonitrile Photon-Upconverted Nanofibers for Optical Temperature Sensors, *ACS Appl. Nano Mater.*, 2023, **6**, 13570–13581.

36 Y. Wang, P. Dang, L. Qiu, G. Zhang, D. Liu, Y. Wei, H. Lian, G. Li, Z. Cheng and J. Lin, Multimode Luminescence Tailoring and Improvement of $Cs_2NaHoCl_6$ Cryolite Crystals via Sb^{3+}/Yb^{3+} Alloying for Versatile Photoelectric Applications, *Angew. Chem., Int. Ed.*, 2023, **62**(45), e20231169.

37 R. Chen, On Calculation of Activation Energies and Frequency Factors from Glow Curves, *J. Appl. Phys.*, 1969, **40**, 570–585.

38 K. Eeckhout, A. Bos, D. Poelman and P. Smet, Revealing trap depth distributions in persistent phosphors, *Phys. Rev.*, 2013, **87**(4), 45126.36.

39 Z. Li, N. Yu, J. Zhou, Y. Li, Y. Zhang, L. Huang, K. Huang, Y. Zhao, S. Kelmar, J. Yang and G. Han, Coloring Afterglow Nanoparticles for High-Contrast Time-Gating Free Multiplex Luminescence Imaging, *Adv. Mater.*, 2020, **32**(49), 2003881.

40 S. Wu, Q. Liu, P. Xiong, W. Chen, Q. Dong, D. Chen, D. Wang, G. Zhang, Y. Chen and G. Li, Single Bi^{3+} Ultrabroadband White Luminescence in Double Perovskite via Crystal Lattice Engineering toward Light-Emitting Diode Applications, *Adv. Opt. Mater.*, 2022, **10**(11), 2102842.

41 Q. Zeng, M. Runowski, J. Xue, L. Luo, L. Marciniak, V. Lavín and P. Du, Pressure-Induced Remarkable Spectral Red-Shift in Mn^{2+}-Activated $NaY_9(SiO_4)_6O_2$ Red-Emitting Phosphors for High-Sensitive Optical Manometry, *Adv. Sci.*, 2024, **11**, 2308221.

42 H. Lv, P. Du, W. Li and L. Luo, Tailoring of upconversion emission in Tm^{3+}/Yb^{3+}-codoped $Y_2Mo_3O_{12}$ submicron particles via thermal stimulation engineering for noninvasive thermometry, *ACS Sustainable Chem. Eng.*, 2022, **10**(7), 2450–2460.

43 G. Kresse and J. Furthmüller, Efficiency of ab-initio total energy calculations for metals and semiconductors using a plane-wave basis set, *Comput. Mater. Sci.*, 1996, **6**(1), 15–50.

44 S. Kurra, N. K. Veldurthi, J. R. Reddy, C. S. Reddy and M. Vithal, A series of novel double perovskite oxides $NaMTi_2O_6$ (M = Eu, Sm, and Gd): preparation, characterization and photocatalytic studies under visible and solar-light irradiation, *J. Mater. Sci.: Mater. Electron.*, 2016, **27**, 4194–4200.

4730 | *Inorg. Chem. Front.*, 2024, **11**, 4721–4730

This journal is © the Partner Organisations 2024